Scientific Reports

https://doi.org/10.1038/s41598-026-44056-9

Article in Press

Comparing UV-enhanced and direct reduction strategies for CD8 T-cell electrochemical detection

Received: 20 December 2025

Accepted: 9 March 2026

Published online: 09 May 2026

Cite this article as: Amoo M., Salimijazi H., Labbaf S. *et al.* Comparing UV-enhanced and direct reduction strategies for CD8 T-cell electrochemical detection. *Sci Rep* (2026). https://doi.org/10.1038/s41598-026-44056-9

Maryam Amoo, Hamidreza Salimijazi, Sheyda Labbaf & Fathallah Karimzadeh

Comparing UV-Enhanced and Direct Reduction Strategies for CD8⁺ T-Cell Electrochemical Detection

Maryam Amoo*, Hamidreza Salimi Jazi*, Sheyda Labbaf, Fathallah Karimzadeh

Department of Materials Engineering, Isfahan University of Technology, Isfahan 84156-83111, Iran

*Corresponding authors: amaryam12@yahoo.com & hrjazi@iut.ac.ir

Abstract

A novel electrochemical biosensor was developed for accurate and sensitive detection of $CD8^+$ T cells, as a key biomarker in clinical and immunological analysis. A screen-printed electrode was modified through 20 cycles of electrodeposition using two approaches: a reduced graphene oxide–polypyrrole composite (A20) and graphene oxide reduced under UV irradiation during polymerization (B20). Characterization analysis indicated that A20 exhibited improved structural uniformity and a higher relative abundance of carboxyl groups compared to B20 sample. These features achieved through a simple and cost-effective fabrication process, significantly improved the electrochemical performance of A20, making it as an optimal sensing platform. The A20-based biosensor detected $CD8^+$ T cells with limit of detection 1.19×10^4 cells.mL^{-1}, which the results aligned with flow cytometry by 97%, confirming its precise accuracy. Further experiments using $CD20^+$, $CD19^+$ and $CD4^+$ cells confirmed the biosensor's selectivity. This study introduces a simple, scalable process for creating composites that greatly enhances the sensitivity of biosensors. Because it is affordable and easy to produce, this biosensor is well-suited for clinical and laboratory use, and also creates opportunities for developing sensors that detect other cellular biomarkers.

Keywords: Biosensor, Reduce graphene oxide (rGO), electrochemical cyclic voltammetry (CV), Differential Pulse Voltammetry (DPV), Ultraviolet (UV), CD8 biomarker

1. Introduction

Recently, the CD8 biomarker has gained significant attention in immunology and oncology due to its crucial role in regulating immune responses through cytotoxic T lymphocytes, or $CD8^+$ T cells. $CD8^+$T cells play a crucial role in targeting infected or cancerous cells, making CD8 an important marker for diagnosis and treatment monitoring[1]. This specificity highlights the importance of CD8 quantification in understanding immune mechanisms involved in various pathological states, such as cancer, infectious diseases, and autoimmune disorders [2,3].

CD8 quantification serves not only in prognostic evaluation but also in guiding therapeutic decisions. The application of $CD8^+$ T cell analysis is particularly impactful and instrumental in oncology as tumor-infiltrating lymphocytes (TILs) [4], chronic viral diseases like HIV and hepatitis C and the overall status of immune function [5], as well as vaccine development [6]. $CD8^+$ T cell dysregulation plays a key role in autoimmune diseases like multiple sclerosis and rheumatoid arthritis, making CD8 an important biomarker for immune profiling and identifying therapeutic targets [7].

Advanced immunological techniques, such as flow cytometry and immunohistochemistry, enable precise quantification and profiling of $CD8^+$ T cells, supporting a better perception of their dynamics and applications in personalized medicine [8]. Flow cytometry is useful for $CD8^+$ T-cell

immunophenotyping but has limited sensitivity for low-frequency populations and is prone to variability due to fluorescence-based measurements. Its extensive sample preparation and high operational costs also restrict its in resource-limited settings [9].

Electrochemical methods, especially differential pulse voltammetry (DPV), offer a sensitive, rapid, and cost-effective approach for detecting low-abundance biomarkers like $CD8^+$ T cells [10,11].

As a whole, $CD8^+$ T cells are key immune biomarkers with significant roles in immunology and oncology, including prognosis, therapeutic monitoring, and assessment of vaccine-induced immunity. Accurate and sensitive detection of these cells is essential for understanding immune responses and guiding personalized therapies. However, traditional detection methods, such as flow cytometry, are often complex, time-consuming, and costly. Hence, electrochemical biosensors, particularly those based on DPV, offer a promising alternative due to their high sensitivity, simplicity, and cost-effectiveness [12].

Several recent studies have developed electrochemical biosensors for detecting various CD markers, each utilizing distinct methodologies, nevertheless, the rare affordable and straightforward preparation strategies have been applied to construct electrochemical biosensors using for clinical and scalable biomedical applications. For example, Carinelli et al [13]. Developed a magnetic electrochemical biosensor for detecting $CD4^+$ T cells with a detection limit of 44 cells.μL^{-1}. This biosensor employed immuno-

magnetic separation and labeling techniques. Despite achieving reliable detection, complex procedures and multiple preparation steps were involved. Similarly, Białas et al. [14] reported an impedance-based biosensor for $CD4^+$ T cell detection, achieving a detection limit of 1.41×10^5 cells.mL^{-1} for $CD4^+$ cells isolated from blood samples.

In another study by Yadegari et al. [15], an electrochemical cytosensor was developed for the ultrasensitive detection of Du-145 prostate cancer cells using modified graphene–gold nanostructures. The sensor achieved a limit of detection (LOD) of 20 cells.mL^{-1}, attributed to the dual recognition by antibodies and the amplification of the enzymatic signal of horseradish peroxidase (HRP). The current study was conducted as an investigation into the optimization of materials for a highly sensitive biosensor. While graphene oxide offers a high density of oxygen-containing functional groups, which are often considered beneficial for bioconjugation, our results demonstrate that the direct use of GO with simultaneous UV-assisted reduction during polymerization does not outperform the pre-optimized Ppy/rGO system.

UV irradiation during polymerization is known to induce partial photoreduction of graphene oxide, leading to its transformation into reduced graphene oxide (rGO) through the removal of epoxy and hydroxyl groups and surface reorganization of oxygen-containing functionalities. Varghese and et.al [16] reports indicate that this UV-assisted

process can enhance the relative accessibility of carboxyl groups on the graphene surface.

Therefore, the primary objective of the present study is to design and fabricate a highly sensitive, reproducible, and economically viable electrochemical biosensor for the quantitative detection of $CD8^+$ T cells based on a differential pulse voltammetry (DPV) platform. This study aims to systematically optimize the electrode composition and surface engineering strategy to enhance signal transduction efficiency and analytical performance. In particular, a comparative evaluation between a pre-optimized polypyrrole/reduced graphene oxide (Ppy/rGO) system and UV-assisted graphene oxide (GO) modification was conducted to elucidate the influence of material properties and reduction approaches on biosensor sensitivity and stability. Ultimately, this work aims to contribute to the development of simplified and potentially scalable electrochemical sensing platforms for $CD8^+$ T cell analysis.

2. Materials and methods

2.1 Material

Pyrrole (S8135392) (98%) with (M=67.09 $g.mol^{-1}$) was supplied by Sigma-Aldrich. Reduced Graphene Oxide powders (rGO) with (99%, 3.4-7 nm) were provided by American Elements. C-GENEO-01-P.REDU, potassium ferrocyanide ($K^4[Fe(CN)_6]$), potassium ferricyanide ($K^3[Fe(CN)_6]$) and Potassium chloride (KCl)7447-45-7 were supplied by Merck, Germany. Anti-Human CD8 Mouse Monoclonal antibody (SB-019972) was provided by

SINA BIOTECH, Iran. $CD8^+$ T cells were prepared at an initial concentration of approximately 5×10^6 cells.mL^{-1} and subsequently subjected to serial dilutions using PBS buffer in room temperature, but $CD8^+$ T cells freeze in -20°C for 1 month. These samples were prepared and provided by the Immunology Laboratory of Isfahan University of Medical Sciences. Bovine serum albumin (BSA) with (A9418-5G) (>96%) and phosphate buffered saline tablets (PBS), ethanol, N-(3-Dimethylaminopropyl)- ethyl carbodiimide hydrochloride (EDC), S7663807 were supplied by Sigma Aldrich, Germany. Moreover, N-Hydroxysuccinimide (NHS) (130672-5G) (98%) were purchased from Sigma Aldrich, Germany. All aqueous solutions were prepared with deionized pure water. Figure 1 shows the schematic illustration of the electrochemical biosensor.

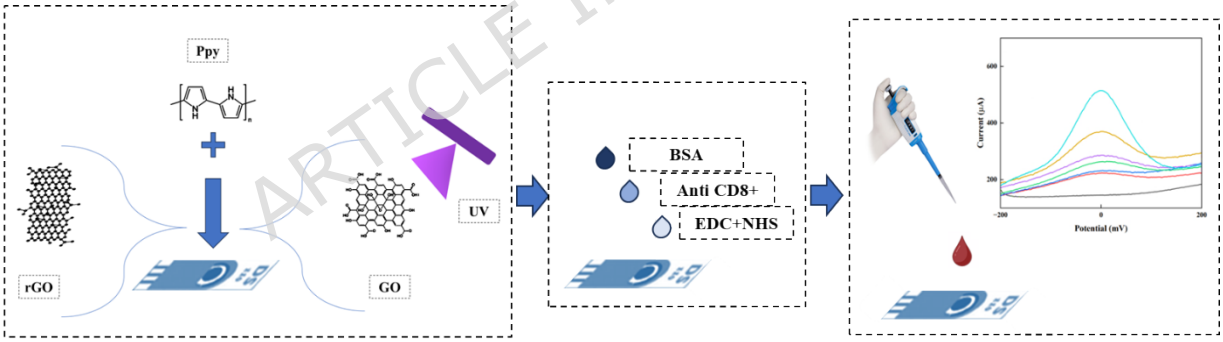

Figure1: schematic illustration of the electrochemical biosensor

2.2 Electrode Preparation

Phase (A), Preparation of Reagents: Two electrolyte formulations were simultaneously prepared for the electrochemical coating process: one based on reduced graphene oxide (rGO) and the another one on graphene oxide

(GO). For the rGO formulation, KCl (0.1 M) was first dissolved in distilled water for 10 minutes to ensure complete solubility, followed by pyrrole (0.025 M) was added to the solution. Having ultrasonicated rGO (0.33 $mg.mL^{-1}$) and PBS (0.05 M) for 15 minutes to achieve uniform dispersion, they were mixed for an additional 20 minutes before being added to the KCl–pyrrole solution. For the GO formulation, GO (0.33 $mg.mL^{-1}$) was dispersed in ethanol and ultrasonicated for 15 minutes to facilitate exfoliation of the sheets. This mixture was stirred magnetically for 20 minutes and then added to the prepared KCl–pyrrole solution. Both final mixtures were stirred magnetically for 30 minutes to ensure homogeneity and subsequently subjected to the electrochemical deposition process [17].

Electrochemical Deposition Process: The electrochemical deposition process was carried out using a Parstat™ Systems Electrochemical Analyzer, enabling precise control of the electrodeposition parameters. Electrochemical measurements, including coating characterization and assessment of uniformity, were subsequently performed using a Parstat™ Systems Electrochemical Analyzer. All experiments were conducted at ambient temperature.

For the electrode fabrication, two approaches were employed. In the first approach, an electrode was prepared using a composite of reduced graphene oxide (rGO) and polypyrrole, which was subjected to 20 cycles of the selected electrodeposition process [18]. In the second approach, an electrode was fabricated by combining graphene oxide (GO) with pyrrole,

followed by exposure to ultraviolet (UV) irradiation (Philips UV lamp, TL 8W BLB, 365 nm) during a cyclic voltammetry deposition. The application of UV light served as a reduction method and was specifically intended to activate the carboxyl functional groups, thereby enhancing composite formation and improving electrode deposition [19]. Among the examined candidates, the optimized electrode material was selected based on detailed characterization via FTIR, FESEM, contact angle, XPS and subsequently utilized in the next step of the study.

Electrodeposition settings, such as polymerization cycles, followed our previously optimized Ppy/rGO method [18]. Twenty cycles were found optimal, yielding a stable, uniform composite with strong electrochemical properties [18]. Here, the optimized condition was maintained to allow a direct comparison under identical experimental conditions between the conventional Ppy/rGO composite and the GO-based system subjected to in situ UV-assisted reduction.

For FTIR analysis, a very small amount of material was gently scraped from the sample surface to avoid altering the overall structure. The collected powder was subsequently used for FTIR measurements.

For contact angle measurement, PBS was chosen due to its compatibility with the subsequent steps of biomarker dissolution and biosensing assays. All experiments were conducted under ambient conditions.

XPS measurements were performed using a BesTek spectrometer (Germany) equipped with a monochromatic Al Kα radiation source (photon energy = 1486.6 eV). The analysis chamber was maintained at a base pressure below 1×10^{-8} mbar. Both survey and high-resolution spectra were acquired to determine the elemental composition and chemical states of the species present on the electrode surface. The recorded spectra were calibrated using the C 1s peak at 284.8 eV as a reference.

All electrochemical measurements were performed in triplicate. To evaluate reproducibility, identical screen-printed electrodes (SPEs) were independently modified and evaluated following the same protocol at approximately one-week intervals. Each modified SPE was tested under identical experimental conditions. The obtained responses showed close agreement, demonstrating good electrode-to-electrode reproducibility. Furthermore, strict adherence to the previously reported fabrication and measurement protocol supports the reproducibility of the proposed sensing approach [18].

Phase (B), Immobilize anti CD8: For the preparation of the electrode for CD8 detection, sequential functionalization steps were performed using EDC/NHS, anti-CD8 antibody, and bovine serum albumin (BSA). At each step, 2 µL of the respective reagent was applied to the electrode surface and incubated for 30 minutes. Following this modification process, the electrode was employed for CD8 detection using DPV. The measurements were conducted in a phosphate buffer solution containing 5 mM

$[Fe(CN)_6]^{3-/4-}$ for each sample. However, for detection at higher concentrations, the DPV analysis were carried out in PBS alone. All human samples were diluted 20-fold prior to measurements.

A series of CD8-positive cell suspensions with defined concentrations were prepared in PBS to evaluate the analytical performance of the biosensor. The tested concentrations ranged from the blank sample (0 cells.mL^{-1}) up to 5.0×10^4 cells.mL^{-1}, including intermediate levels of 10, 20, 40, 80, 3.2×10^2, 1.0×10^3, 1.0×10^4, 2.0×10^4, and 2.5×10^4 cells.mL^{-1}. Each concentration was assigned an individual sample code corresponding to its cell density, enabling systematic assessment of sensor response across a broad dynamic range.

CD8+ T cells were stabilized on the electrode surface after 30 min incubation. Even if cell viability decreases during the short-term (~2 min) DPV test, physical cell attachment remains stable, consistent with short-term electrochemical cytotoxicity assays[20].

Electrochemical characterization followed optimized protocol of Amoo et al. [18] for Ppy/rGO immunosensors: The test substrate comprised 0.1 M PBS (pH 7.4) containing, providing physiological pH for optimal biorecognition and stable redox probe signal. Antibody immobilization was performed for 30 minutes at 25°C (room temperature).

2.3 Characterization

A comprehensive microstructural analysis was conducted; surface wettability was evaluated through the droplet method by CA-500A and fourier-transform infrared (FTIR, Tensore27) was used for chemical analysis. The surface morphology of the prepared samples was characterized using field-emission scanning electron microscopy (FESEM; Quanta FEG 450, FEI, Netherlands). Prior to imaging, the samples were sputter-coated with a thin gold layer to enhance electrical conductivity and minimize surface charging. High-resolution FESEM micrographs were subsequently acquired at an accelerating voltage of 10 kV. The surface wettability of the samples was assessed using the sessile droplet method with a contact angle measurement system (CA-500A, Kyowa Interface Science Co., Japan). A droplet of deionized water was carefully dispensed onto the sample surface at room temperature, and the contact angle was recorded immediately.

3. Result and discussion

3.1 FTIR analysis

The FTIR spectra for samples A20 and B20 show clear differences in vibrational patterns in figure 2, indicating notable variations in surface chemistry and functional group signatures. Sample A20 exhibits three dominant absorption features at 3445 cm^{-1}, 2925 cm^{-1}, and 1630 cm^{-1}, each characteristic of distinct vibrational modes [21]. The broad band

centered at 3445 cm^{-1} arises from strongly hydrogen-bonded O–H stretching vibrations, suggesting the presence of surface hydroxyl groups and hydrogen-bonding interactions, potentially associated with adsorbed water or hydroxylated surface states. The peak at 2925 cm^{-1} corresponds to aliphatic C–H asymmetric stretching, suggesting the incorporation of hydrocarbon-based organic moieties or residual carbonaceous species distributed across the matrix. Meanwhile, the absorption at 1630 cm^{-1} can be attributed to C=O stretching or H–O–H bending associated with molecularly trapped water or carbonyl-containing functionalities, highlighting the presence of oxygenated species and intermediate oxidation domains [22].

In contrast, sample B20 displays a largely featureless spectral profile across the same wavenumber region, characterized by the absence of functional group signatures observed in A20. The suppression of these vibrational modes indicates a reduced contribution from surface hydroxyl groups, organic components, and molecularly associated water, leading to a comparatively lower overall vibrational activity. The marked reduction in B20 may be associated with UV-assisted chemical modification and partial removal or transformation of labile functional groups, while the spectral pattern of A20 remains dominated by oxygen- and carbon-related vibrations [23].

Overall, these FTIR results provide molecular-level evidence of significant chemical modification between A20 and B20, primarily reflected in changes

in functional group presence and vibrational intensity. The spectral differences are interpreted as arising from variations in surface functionalization, hydrogen-bonding interactions, and local chemical environments, which are consistent with the observed electrochemical and surface characterization results.

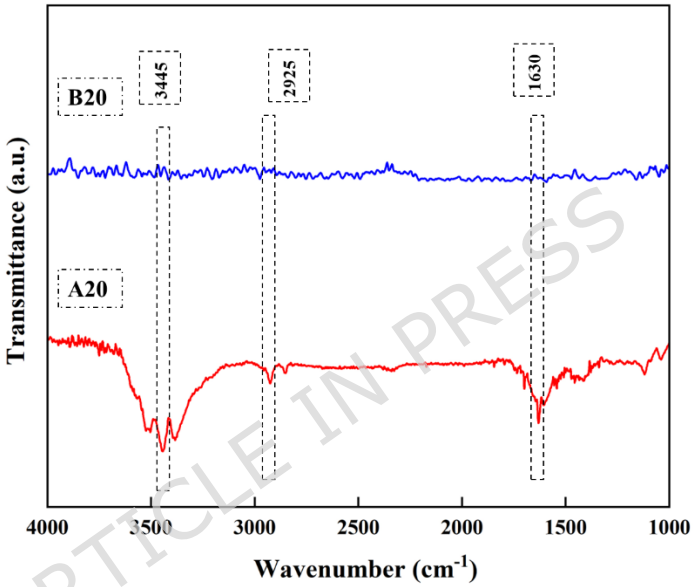

Figure 2: Comparing the FTIR spectra of sample A20 with B20

In the FTIR spectrum, characteristic bands at 3445 cm^{-1}, 2925 cm^{-1}, and 1630 cm^{-1} correspond to N–H stretching, C–H stretching, and C=C stretching within the conjugated polymer backbone, respectively, confirming the formation of its pyrrolic and conjugated structure [24-27].

Reduced graphene oxide (rGO), resulting from the partial removal of surface oxygen-containing groups, exhibits high electrical conductivity and a large active surface area. These properties enable rGO to serve as a

conductive enhancer within bio-sensing platforms, amplifying electrochemical signals and improving detection sensitivity. Its porous structure facilitates interaction with biomolecules, including proteins and antibodies, thereby enhancing sensor selectivity and precision in detecting targets such as $CD8^+$ T cells [24,28].

3.2 Morphological Analysis via FESEM

Figure 3 shows the FESEM images of A20 sample. The observed cauliflower-like structures are characteristic of polypyrrole [29], whereas the sheet-like morphologies correspond to graphene oxide layers [30]. At various magnifications, FESEM images reveal a uniform coating of polypyrrole over reduced graphene oxide sheets, indicating effective integration of the two components. The presence of surface pores and hierarchical porosities is a biomarker capturing efficiency by increasing the specific surface area and providing abundant active sites for biomolecular interactions. These structural features are expected to facilitate improved analyte adsorption, enhance charge transfer kinetics, and ultimately optimize the sensitivity and performance of the biosensing platform [31,32]. This phenomenon was reported by Hu and et.al [31] in the previous study and demonstrated that a three-dimensional porous rGO/Ppy composite exhibited superior biosensing performance due to the optimized surface area and enhanced electron transfer capabilities.

To further investigate the cross-sectional morphology of samples, additional FESEM images are taken at a 45-degree tilt angle and it shows in figure 3-C

and 3-D. These images reveal a layered integration of polypyrrole and reduced graphene oxide, confirming the formation of a stratified hybrid structure. This layered configuration is expected to enhance the electron transport pathways and improve the overall electrochemical performance of the bio-sensing platform [29,30].

Figures 3-E and 3-F shows the FESEM images of the B20 and SPE samples. Microstructures confirm that a well-integrated hybrid structure of polypyrrole and reduced graphene oxide has not been successfully formed. The observed morphology predominantly consists of reduced graphene oxide sheets, while polypyrrole appears to have been removed during the washing process, indicating insufficient adhesion or stability within the composite structure [33].

Figure 3-E reveals the characteristic sheet-like structure of graphene oxide, which becomes more pronounced at higher magnifications (Figure 3-F), further confirming the lack of a homogeneously distributed polymeric network. Reduced graphene oxide, owing to its extensive surface area enables efficient biomolecule immobilization, and polypyrrole, through its capability to enhance electron-transfer processes, typically imparts complementary functional contributions within these systems [34,35].

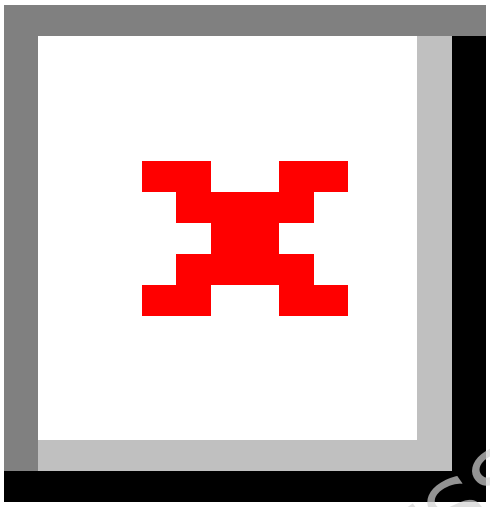

Figure 3: FESEM images of sample A20. A) 10µm and B) 5 µm magnifications. FESEM analysis of sample A20 (tilt 45º). C) 1mm and D) 1µm, magnifications. FESEM Images of B20. E) 10µm, and F) 5µm, magnifications

Furthermore, FESEM images reveal pronounced morphological differences between the A20 and B20 composites. The A20 sample exhibits a three-dimensional, loosely stacked architecture with abundant inter-sheet voids, whereas B20 shows densely packed rGO sheets with limited accessible void space. The pore size distribution and average pore diameter were also measured using FESEM image. It should be noted that pore size was

estimated based on inter-sheet voids observed in FESEM images rather than intrinsic microporosity. The analysis indicates that the characteristic pore sizes are on the order of approximately 1–2 µm. At comparable magnification (10 µm scale), the pore density and average pore size observed in image A are noticeably higher than those in Figure 3-B. Furthermore, ImageJ-based analysis reveals that the average pore size in A20 is approximately five times larger than that estimated for B20 (Figure 3-E). This semi-quantitative analysis provides a reliable comparison of the accessible porous structure relevant to electrochemical and biosensing performance. The larger and more abundant inter-sheet voids in A20 are consistent with its enhanced electrochemical response and improved sensing sensitivity.

3.3 Contact Angle

Figure 4 illustrates the wettability characterization and comparative analysis of the contact angle measurements for samples A20 and B20. The measured contact angle for substrate A20 is approximately 112°, while that of B20 reaches about 134°. These results suggest a reduced surface hydrophilicity in sample B20 relative to A20, potentially affecting its biomolecular interaction and adsorption behavior in downstream applications. Under ultraviolet (UV) irradiation, the surface of graphene oxide (GO) undergoes a reduction of oxygen-containing groups such as carboxyl (-COOH) and hydroxyl (-OH). These oxygen-containing groups impart hydrophilic properties to the GO surface due to their polar nature.

Upon their removal, particularly through photochemical or photocatalytic processes, the surface gradually transitions to a hydrophobic state. This transition is evidenced by an increase in the water contact angle on the sample surface [36].

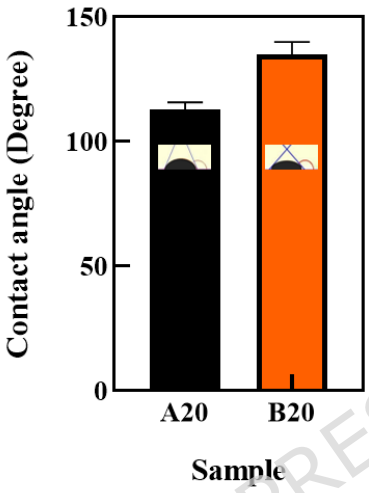

Figure 4: Contact angle measurements

Graphene oxide (GO), possesses oxygen-containing functional groups such as hydroxyl (–OH), epoxy (–O–), and carboxyl (–COOH) on its basal planes and edges. These polar groups render GO highly hydrophilic, enabling good dispersion in aqueous media and promoting interfacial reactivity. During reduction, many of these oxygen functionalities are removed, increasing electrical conductivity and producing a structure closer to pristine graphene. However, some oxygen groups remain on the rGO surface, maintaining partial hydrophilicity and allowing hydrogen-bond interactions and analyte adsorption. This balance between conductivity enhancement and surface hydrophilicity is crucial for optimizing rGO's interfacial performance in sensing applications [24,26]. Higher surface hydrophilicity can

increase the contact area between the solution and the surface, potentially enhancing antibody immobilization and overall sensor performance.[37]

FESEM, FTIR, and water contact angle analyses were employed to evaluate the reproducibility of the A20 composite coating. As illustrated in Figure 3, FESEM images of A20 recorded at different magnifications (10 µm, 5 µm, and 1 µm), as well as tilted-view imaging (45°), revealed a homogeneous morphology composite distribution across the electrode surface.

The reproducibility of the surface modification was further supported by FTIR spectra, which exhibited consistent characteristic absorption bands corresponding to the A20 composite, confirming uniform chemical composition. Additionally, water contact angle measurements showed consistent values with low deviation for independently fabricated electrodes, indicating stable and uniform surface wettability.

3.4 XPS Analysis

XPS was employed to further investigate the surface chemical composition of the fabricated electrodes and to complement the FTIR, FESEM, and contact angle analyses. Figure 5 shows the normalized XPS survey spectra of A20 (Ppy/rGO) and B20 (Ppy/GO with UV-assisted in situ reduction), providing an overview of the surface elemental composition.

The survey spectra of both samples are dominated by the characteristic core-level peaks of carbon (C 1s, ~284 eV), nitrogen (N 1s, ~399 eV), and oxygen (O 1s, ~532 eV), confirming the successful formation of the Ppy-based composite layer on the electrode surface. For clarity, only these

principal core-level peaks are labeled in the survey spectra, as they are directly relevant to the surface chemistry of the sensing interface [38].

A comparative inspection of the survey spectra indicates similar elemental features for A20 and B20, suggesting that the overall surface composition is not markedly altered using graphene oxide and UV-assisted reduction during the polymerization process. This observation is consistent with the comparable electrochemical responses observed for the two electrodes.

To gain further insight into the surface functional groups, high-resolution C 1s analysis was considered. The deconvoluted C 1s spectrum of A20 has been previously reported[18] in our earlier work using the same fabrication protocol. In the present study, the high-resolution C 1s spectrum of B20 was analyzed using identical fitting procedures, allowing a direct and meaningful comparison. The fitted C 1s components correspond to C–C/C=C (~284.6 eV), C–O/C–N (~286.2 eV), C=O (~287.8 eV), and O–C=O (~288.8–289.2 eV) functionalities.

The C 1s analysis reveals that, despite the higher initial density of oxygen-containing functional groups in graphene oxide, the UV-assisted in situ reduction process does not result in a substantial increase in surface carboxyl functionalities compared to the pre-optimized Ppy/rGO composite. This finding indicates that the preservation of electronic conductivity and controlled reduction state play a more critical role in determining the

interfacial properties of the cytosensor than functional group density alone [39].

Overall, the XPS results support the conclusions drawn from electrochemical and biosensing experiments and provide additional evidence that UV-assisted reduction of GO during polymerization does not offer a clear surface chemical advantage over the previously optimized Ppy/rGO system.

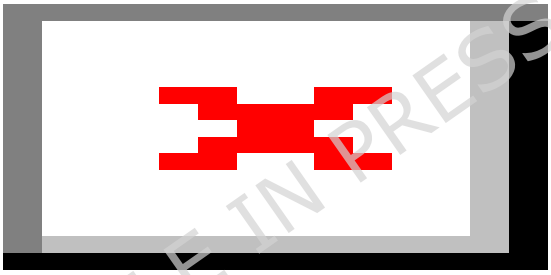

Figure 5: XPS spectrum of sample A20 and B20: A) survey, B) B20: C1s.

3.5 Mechanistic Insights into EDC/NHS-Mediated Bio-Conjugation on the Ppy/rGO Interface

To achieve selective bio-functionalization of the modified electrode surface, phase (B) is designed based on the EDC/NHS carbodiimide activation strategy. In the first step, EDC reacts with the surface-exposed carboxyl (–COOH) groups to form an unstable O-acylisourea intermediate, which

rapidly undergoes hydrolysis in aqueous media unless stabilized by NHS [40,41]. Upon the addition of NHS, this intermediate is converted into a more stable NHS-ester that remains reactive toward primary amines for an extended period [40]. Subsequently, this activated ester undergoes nucleophilic substitution with the amine groups of the anti-CD8 antibody—primarily located on surface lysine residues—leading to the formation of a covalent amide bond. This process establishes a stable and efficient attachment of the antibody onto the composite-modified surface [42].

In the fabricated sensing platform, the conductive substrate consists of a screen-printed carbon electrode coated with a Ppy/rGO composite layer. Polypyrrole, owing to its high electrical conductivity (typically in the range of 1 to 1000 S/cm) and its conjugated backbone, significantly enhances electron-transfer processes and amplifies the electrochemical response [43,44]. Meanwhile, reduced graphene oxide provides a high density of active sites that improves biomolecular interactions, molecular adsorption, and the overall analytical performance of the sensing interface. The combination of these two materials creates a strong synergistic effect that markedly enhances the sensitivity and functionality of the biosensor.

Following the bio-conjugation of anti-CD8, the sensing performance is evaluated using DPV for the highly sensitive and precise detection of CD8+ T cells. Considering the limitations of conventional techniques such as flow cytometry—and the advantages of electrochemical methods, including low cost, rapid analysis, and suitability for point-of-care applications—this

approach offers an efficient and reliable strategy for detecting this clinically significant biomarker [33,45].

3.6 DPV analysis

Figure 6 presents the DPV results of samples, with panel (A) displaying the DPV responses at low concentrations, allowing for precise evaluation of the sensor sensitivity, and panel (B) depicting the responses at higher concentrations to assess the sensor performance under the saturated conditions. The low-concentration measurements are conducted in the $[Fe(CN)_6]^{3-/4-}$ solution to ensure accurate electrochemical characterization, while the high-concentration measurements are performed in PBS, simulating physiological conditions and providing insights into the sensor potential for biomedical applications [46,47].

With increasing biomarker concentration, the binding of CD8 molecules increases, leading to a decrease in the current response (Figure 6-A). This phenomenon indicates an increase in the electrode resistance.

The DPV response of the fabricated biosensor was evaluated as a function of $CD8^+$ T-cell concentration. As illustrated in the calibration curve, the peak current decreases progressively with increasing cell concentration, which can be attributed to enhanced surface blocking and reduced electron-transfer efficiency caused by the attachment of cells onto the electrode surface.

A linear relationship was observed when the DPV current (mA) was plotted against the logarithm of cell concentration (cells.mL^{-1}), yielding a

coefficient of determination (R^2) of 0.7. This level of correlation is considered reasonable for whole-cell electrochemical biosensing systems, where biological variability and non-ideal surface interactions are inherently present.

The negative slope of the semi-logarithmic calibration curve (–0.13 mA per decade) indicates that for each tenfold increase in cell concentration, the DPV current decreases by approximately 0.13 mA, reflecting the sensitivity of the biosensor toward $CD8^+$ T-cell detection. Given the complexity of cell–surface interactions, a semi-log linear model was employed to describe the experimental trend without over-interpreting binding parameters.

Furthermore, taking advantage of this sensitivity, the limit of detection (LOD) can be calculated using the following formula [48,49]:

$$LOD = 3 \times SD_{blank} / S \quad (2)$$

where SD represents the standard deviation of the output current for the 0 cell sample and S is the slope of the calibration curve [50].

The DPV response of the biosensor was evaluated as a function of $CD8^+$ T-cell concentration. As shown in the calibration curve, the peak current decreases systematically with increasing cell concentration, which can be attributed to progressive surface blocking and hindered electron transfer caused by cell attachment on the electrode surface.

When the DPV current was plotted against the logarithm of cell concentration (cells mL^{-1}), a semi-logarithmic linear relationship was observed, yielding a coefficient of determination (R^2) of 0.7. This level of correlation is considered reasonable for whole-cell electrochemical biosensing systems, where inherent biological variability and non-ideal surface interactions are expected.

The negative slope of the calibration curve (–0.13 A per decade) indicates that for each decade increase in cell concentration, the DPV current decreases by approximately 0.13 A, reflecting the sensitivity of the sensor toward $CD8^+$ T-cell detection. Using the standard deviation of the blank (SD_{Blank} = 514.56 A), the LOD was calculated as (2), resulting in an LOD of approximately 1.19×10^4 cells.mL^{-1}.

On the other hand, Figure 6-B presents the DPV response at higher cell concentrations. In this regime, the progressive accumulation of cells on the electrode surface substantially limits the effective electroactive area and suppresses the redox activity probed during the potential pulses. As the number of surface-bound cells increases, the accessibility of the electrode to the supporting redox species decreases, resulting in a concentration-dependent attenuation of the peak current. This behavior yields a clear inverse linear trend, expressed by I = –2E-07 N + 0.12 (R^2 = 0.98).

The reduction in DPV peak height at elevated concentrations is consistent with dominant surface-blocking effects commonly reported in cell-based

electrochemical assays. Extensive cell coverage hampers charge-transfer events by shielding conductive domains, increasing local mass-transport limitations within the thin diffusion layer sampled during the DPV pulses, and diminishing the effective flux of electroactive species to the electrode interface. Consequently, the pulsed measurement registers a markedly reduced faradaic current.

Overall, the observed decrease in peak intensity directly reflects the extent of cell-induced surface obstruction and aligns with the classical surface-fouling mechanism described for DPV-based biosensors at high analyte loading [51].

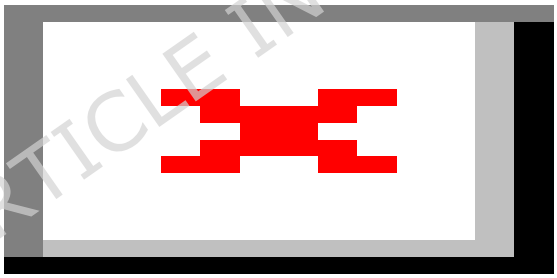

Figure 6. DPV responses obtained from triplicate measurements for different concentration ranges: (A) 0–1000 cell mL^{-1} and (B) 10,000–50,000 cell mL^{-1}.

Electrode stability in the $[Fe(CN)_6]^{3-/4-}$ redox probe during static DPV measurement ensures results are independent of live/dead cell status, as reported in electrochemical biosensor-based viability monitoring [20,52]. Tests

were conducted at high concentrations approximating human physiological conditions in PBS buffer.

While the reproducibility of the sensor fabrication was rigorously confirmed using three independently prepared electrodes (Figure 6), long-term stability studies were not conducted. This is due to the storage constraint of the antibody component, which requires –20 °C to maintain its activity. Consequently, the sensor is designed as a single-use disposable platform for immediate application after assembly to ensure measurement reliability. Assessments over extended storage periods are not feasible within this design framework, a limitation that aligns with reports for similar antibody-based biosensors [19,53].

A detailed electrochemical analysis of Ppy/rGO-modified electrodes—using cyclic voltammetry and electrochemical impedance spectroscopy—was presented in our group's recent publication Amoo et al.[18] This study thoroughly examined optimal electrodeposition cycles and interfacial charge transfer properties. For the current research, we selected modification parameters according to those previously optimized conditions. Therefore, the electrochemical performance was primarily evaluated using differential pulse voltammetry, which is a more suitable for analytical applications. The enhanced DPV peak current observed for the modified electrodes compared to the bare electrode confirms the effective electrochemical activity and favorable interfacial properties of the composites.

3.7 Comparative Analysis of CD8⁺ T-Cells in Human Samples Using DPV, Enhanced Biosensing, and Flow Cytometry Techniques

This study conducts a comparative evaluation of CD8⁺ T-cell quantification in human samples using DPV–based electrochemical biosensing in parallel with conventional flow cytometry. By leveraging the ultrasensitive signal-resolution capabilities of DPV alongside the well-established phenotypic specificity of flow cytometry, the integrated analytical framework enables a robust and multidimensional assessment of CD8⁺ T-cell detection. As summarized in Table 1, the findings delineate the respective strengths and inherent constraints of both modalities—ranging from sensitivity, dynamic range, and surface marker selectivity to operational throughput and clinical translatability—thus providing critical insights into their potential roles within immunological diagnostics and translational biomedical research.

Table 1: Comparison and result of recovered CD8+ T-Cell

Sample	Flowcytometry Concentration (cell.mL^{-1})	Electrochemical Concentration (cell.mL^{-1})	Recovery (%)
H1	5650	5529	97 ± 2
H2	2800	2874	96 ± 1
H3	3090	3211	96 ± 1

H4	4220	4355	96 ± 2

Recovery percentages are presented as mean ± SD, with three independent measurements for each concentration.

In the present study, four independent human samples were analyzed to evaluate the agreement between the proposed biosensor and flow cytometry. Although this sample size does not constitute full clinical validation, it is consistent with previously reported cross-platform comparison studies in cytometry that employed four donors for preliminary performance assessment and method concordance analysis. Therefore, the current results should be interpreted as a proof-of-concept and early feasibility evaluation. Larger cohorts will be included in future investigations to further establish clinical accuracy, reproducibility, and diagnostic robustness.

3.8 Selectivity

To rigorously evaluate the selectivity of the CD8-targeted biosensing platform, two immunologically distinct surface biomarkers $CD4^+$, $CD19^+$ and $CD20^+$ cells are employed as non-target analytes [54,55]. These markers, characteristic of T-helper and B-lymphocyte lineages, respectively, provide a stringent model for assessing the sensor’s capability to discriminate among structurally and functionally divergent cell-surface proteins [56,57].

Electrochemical measurements were carried out under strictly controlled and identical experimental conditions, including fixed analyte concentrations, defined contact periods, uniform buffer composition, and a standardized detection protocol. The sensor generated a pronounced and well-defined electrochemical response in the presence of the $CD8^+$T cell-specific biomarker, whereas signals recorded for $CD4^+$, $CD19^+$ and $CD20^+$ cells remained minimal and within the range of nonspecific background activity (Figure 7).

The observed superior selectivity can be attributed to several key factors: (i) the preserved orientation and functional integrity of the immobilized recognition molecules, (ii) the minimized nonspecific adsorption enabled by the optimized surface modification strategy, and (iii) the efficient electron-transfer properties of the transduction layer, which selectively amplify target-dependent binding events.

In general, these findings confirm that the developed biosensor possesses clear qualitative discrimination toward $CD8^+$T cells-related biomarkers, establishing its suitability for demanding analytical applications such as precise immunophenotyping, targeted cellular profiling, and multiplex biomarker detection within complex biological matrices.

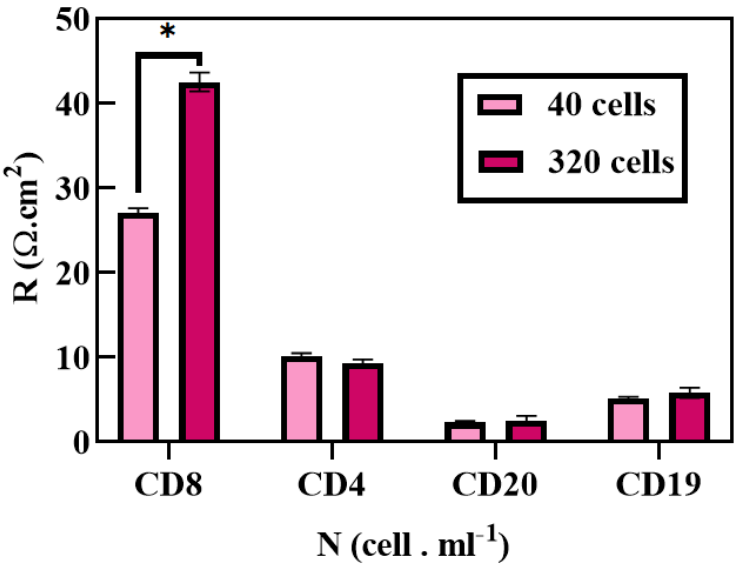

Figure 7: Selectivity of the sensor in detecting $CD8^+$, $CD4^+$, $CD20^+$, and $CD19^+$ cells. (*P<0.05)

These redox-active features, together with the conjugated backbone and N–H functional groups, enhance the molecular recognition capability of polypyrrole. The polymer can interact selectively with target biomolecules through electrostatic interactions, hydrogen bonding, and dopant-dependent charge compensation mechanisms. Such interactions reduce nonspecific adsorption and improve the discrimination of the sensing interface against structurally similar interfering species. As a result, polypyrrole significantly contributes to the overall selectivity of the biosensor, enabling reliable detection of specific biomarkers even in complex biological environments [25,26].

The selectivity of the biosensor was demonstrated against $CD4^+$, $CD19^+$, and $CD20^+$ cells, with results showing clear qualitative discrimination of $CD8^+$ T-cells; more extensive quantitative analysis will be explored in future studies.

4. Conclusions

This study investigated the optimization of an electrochemical cytosensing platform based on a reduced graphene oxide–polypyrrole (rGO/Ppy) modified screen-printed electrode for the detection of $CD8^+$ T cells. The work focused on comparing two fabrication strategies rather than introducing a new sensing concept. Among the evaluated configurations, the directly reduced composite (A20) exhibited more homogeneous surface morphology, improved wettability, and more stable electrochemical behavior compared with the UV-assisted reduction approach (B20). These physicochemical characteristics were associated with enhanced signal stability and sensitivity in differential pulse voltammetry measurements.

The A20-based sensor achieved a limit of detection of 1.19×10^4 cells.mL^{-1} and demonstrated approximately 97% agreement with flow cytometry measurements under the tested conditions. Selectivity experiments against $CD20^+$ and $CD4^+$ cells further supported the specificity of the platform for $CD8^+$ T cell detection. In contrast, the UV-assisted in situ reduction strategy did not yield measurable improvements in electron-transfer kinetics or biosensing performance, despite the higher density of oxygen-containing

groups typically associated with graphene oxide. These findings suggest that enhanced surface functionalization alone does not necessarily translate into improved cytosensing efficiency; rather, a balanced combination of electrical conductivity, interfacial charge-transfer properties, and controlled surface chemistry appears to be more influential.

Overall, the results indicate that the pre-optimized Ppy/rGO configuration remains the more effective architecture within the investigated design space. The study provides experimental evidence supporting the selection of direct reduction over UV-assisted in situ reduction for this specific application. The findings should be interpreted within the scope of a proof-of-concept investigation. Although the sensor exhibited reproducible responses under controlled laboratory conditions, several limitations remain. The current protocol involves manual preparation steps and single-use electrodes, which may limit throughput. Long-term stability of the fully assembled sensor was not assessed, and broader validation in complex biological matrices, including whole blood, is required. Furthermore, systematic comparison with multiparametric flow cytometry across larger sample cohorts would be necessary before considering clinical translation. Within these boundaries, the proposed platform represents a simplified and cost-conscious approach for electrochemical $CD8^+$ T cell detection, with potential adaptability to other cell-surface biomarkers following appropriate validation and optimization.

Ethics Statement

This research was conducted in accordance with ethical principles and research standards (IR.UIT.REC.1403.006). (https://ethics.research.ac.ir/IR.UIT.REC.1403.006)

Funding

This research received no external funding.

Competing interests

The authors declare no competing interests.

5. References

1 Lin, Y. *et al.* Immunometabolic Targets in CD8+ T Cells within the Tumor Microenvironment of Hepatocellular Carcinoma. *Liver Cancer*. **14**, 1-30 (2024).

2 Yost, K. E. *et al.* Clonal replacement of tumor-specific T cells following PD-1 blockade. *Nat. Med.* **25**, 1251-1259 (2019).

3 Jia, J. *et al.* Comprehensive immune landscape of lung-resident memory CD8(+) T cells after influenza infection and reinfection in a mouse model. *Front. Microbiol.* **14**, 1-13 (2023).

4 Martinez, M. & Moon, E. K. CAR T Cells for Solid Tumors: New Strategies for Finding, Infiltrating, and Surviving in the Tumor Microenvironment. *Front. Immunol.* **10**, 1-21 (2019).

5 Nasser Gholijani, G. D., Fatemeh Rezaei Kahmini. T cell-Intrinsic Peripheral Tolerance: A Checkpoint Target to Treat Autoimmunity. *J. Cell. Immunol.* **6**, 87-97 (2024).

6 van de Sandt, C. E. *et al.* Gradual changes within long-lived influenza virus-specific CD8(+) T cells are associated with the loss of public TCR clonotypes in older adults. *EBioMedicine.* **115**, 1-16 (2025).

7 van der Leun, A. M., Thommen, D. S. & Schumacher, T. N. CD8(+) T cell states in human cancer: insights from single-cell analysis. *Nat. Rev. Cancer.* **20**, 218-232 (2020).

8 Chen, Z. *et al.* Immune profiling identifies CD8(+) T-cell subset signatures as prognostic markers for recurrence in papillary thyroid cancer. *Front. Immunol.* **13**, 1-18 (2022).

9 Dror Levinsky, M. *et al.* A Highly Sensitive Flow Cytometric Approach to Detect Rare Antigen-Specific T Cells: Development and Comparison to Standard Monitoring Tools. *Cancers.* **15**, 1-19 (2023).

10 Bertolini, M., Wong, M. S., Mendive-Tapia, L. & Vendrell, M. Smart probes for optical imaging of T cells and screening of anti-cancer immunotherapies. *Chem. Soc. Rev.* **52**, 5352-5372 (2023).

11 Gorjizadeh Kohvade, A., Rajabi, H. R., Roushani, M., Elhamifar, D. & Dadvar, F. An ultrasensitive and selective electrochemical biosensor for Escherichia coli based on bacteria-imprinted polydopamine and a magnetic nanocomposite modifier. *Sci. Rep*. **15**, 1-13 (2025).

12 Hussein, H. A., Hanora, A., Solyman, S. M. & Hassan, R. Y. A. Designing and fabrication of electrochemical nano-biosensor for the fast detection of SARS-CoV-2-RNA. *Sci. Rep.* **13**, 1-11 (2023).

13 Carinelli, S., Xufre Ballesteros, C., Marti, M., Alegret, S. & Pividori, M. I. Electrochemical magneto-actuated biosensor for CD4 count in AIDS diagnosis and monitoring. *Biosens. Bioelectron* .**74**, 974-980 (2015).

14 Bialas, K. *et al.* Electrochemical microfluidic biosensor for the detection of CD4(+) T cells. *Microsyst. Nanoeng.* **11**, 1-13 (2025).

15 Yadegari, A., Omidi, M., Yazdian, F., Zali, H. & Tayebi, L. An electrochemical cytosensor for ultrasensitive detection of cancer cells using modified graphene–gold nanostructures. *RSC Adv.* **7**, 2365-2372 (2017).

16 Varghese, A. M. *et al.* Enhancing effect of UV activation of graphene oxide on carbon capture performance of metal-organic framework / graphene oxide hybrid adsorbents. *Chem. Eng. J.* **420**, 129677 (2021).

17 Seenivasan, R., Chang, W.-J. & Gunasekaran, S. Highly Sensitive Detection and Removal of Lead Ions in Water Using Cysteine-Functionalized Graphene Oxide/Polypyrrole Nanocomposite Film Electrode. *ACS Appl. Mater. Interfaces.* **7**, 15935-15943 (2015).

18 Amoo, M., Salimijazi, H., Labbaf, S., Karimzadeh, F. & Baradaran, A. A sensitive electrochemical immunosensor with Ppy/rGO composite for the detection of CD8+ T cells in blood. *Microchem. J.* **221**, 116788 (2026).

19 Ana Díaz-Fernandez, E. B., Carlos Fernandez-Ramos, Sandhya Moise, Pedro Estrela, Mirella Di Lorenzo. An impedimetric immunosensor for the selective detection of CD34+ T-cells in human serum. *Sens. Actuators B Chem.* **356**, 1-7 (2022).

20 Koo, K.-M. *et al.* Recent Advances in Electrochemical Biosensors for Monitoring Animal Cell Function and Viability. *Biosensors.* **12**, 1162 (2022).

21 Parayangattil Jyothibasu, J., Chen, M. Z. & Lee, R. H. Polypyrrole/Carbon Nanotube Freestanding Electrode with Excellent Electrochemical Properties for High-Performance All-Solid-State Supercapacitors. *ACS Omega.* **5**, 6441-6451 (2020).

22 Zhao, J. *et al.* Enhancing the mechanical and electrochemical properties of reduced graphene oxide composites films through the combined actions of chitosan and polypyrrole. *Carbon.* **231**, 119715 (2025).

23 Seema, S. & Prasad, M. V. N. A. Dielectric Spectroscopy of Nanostructured Polypyrrole-NiO Composites. *J. Polymers.* **2014**, 1-5 (2014).

24 Sanmugam, A. *et al.* Unveiling the PEDOT-polypyrrole hybrid electrode for the electrochemical sensing of dopamine. *Sci. Rep.* **15**, 10989 (2025).

25 Patra, S., Sahu, K. M., Reddy, A. A. & Swain, S. K. Polymer and biopolymer based nanocomposites for glucose sensing. *Int. J. Polym. Mater. Polym. Biomater.* **73**, 490-521 (2023).

26 Kaur, G., Kaur, A. & Kaur, H. Review on nanomaterials/conducting polymer based nanocomposites for the development of biosensors and electrochemical sensors. *Polym.-Plast. Technol. Mater.* **60**, 504-521 (2020).

27 Jain, R., Jadon, N. & Pawaiya, A. Polypyrrole based next generation electrochemical sensors and biosensors: A review. *TrAC Trends Anal. Chem.* **97**, 363-373 (2017).

28 Krishnan, S. K., Singh, E., Singh, P., Meyyappan, M. & Nalwa, H. S. A review on graphene-based nanocomposites for electrochemical and fluorescent biosensors. *RSC Adv.* **9**, 8778-8881 (2019).

29 Das, M. & Roy, S. Polypyrrole and associated hybrid nanocomposites as chemiresistive gas sensors: A comprehensive review. *Mater. Sci. Semicond. Process.* **121**, 105332 (2021).

30 Ma, L., Liu, R., Niu, H., Zhao, M. & Huang, Y. Flexible and freestanding electrode based on polypyrrole/graphene/bacterial cellulose paper for supercapacitor. *Compos. Sci. Technol.* **137**, 87-93 (2016).

31 Hu, J., Li, Y., Gao, G. & Xia, S. A Mediated BOD Biosensor Based on Immobilized B. Subtilis on Three-Dimensional Porous Graphene-Polypyrrole Composite. *Sensors.* **17**, 2594 (2017).

32 Yang, Y. *et al.* Porous conducting polymer and reduced graphene oxide nanocomposites for room temperature gas detection. *RSC Adv.* **4**, 42546-42553 (2014).

33 Ravikiran, Y. T. *et al.* Polypyrrole/reduced graphene oxide composite as a low-cost novel sensing material for fast-response humidity sensor. *Mater. Chem. Phys.* **303**, 127800 (2023).

34 Janmanee, R. & Sriwichai, S. Development of an Electrochemical Biosensor Based on Polypyrrole-3-carboxylic Acid/Polypyrrole/Au Nanoparticle Composites for Detection of Dopamine. *Polymers.* **17**, 1-17 (2025).

35 Babak Mikaeeli Kangarshahi, S. S., Hossein Daneshgar, Mojtaba Bagherzadeh, Seyed Morteza Naghib, Navid Rabiee. Electroconductive polymer-based biosensors for early cancer detection via liquid biopsy: Advances, challenges, and future prospects. *TrAC Trends Anal. Chem.* **183**, 118062 (2025).

36 Li, J., Qi, X., Hao, G., Ren, L. & Zhong, J. In-situ investigation of graphene oxide under UV irradiation: Evolution of work function. *AIP Adv.* **5**, 1-6 (2015).

37 Ghasemi, Z., Salimi Jazi, H., Kharaziha, M., Raeissi, K. & Karimzadeh, F. A freestanding electrochemical sensor based on surface molecularly imprinted polydopamine for glucose detection. *Surf. Interfaces.* **62**, 1-12 (2025).

38 Dey, A., Ghosh, P., Bowen, J., Braithwaite, N. S. J. & Krishnamurthy, S. Engineering work function of graphene oxide from p to n type using a low power atmospheric pressure plasma jet. *Phys. Chem. Chem. Phys.* **22**, 7685-7698 (2020).

39 Cai, C. *et al.* Highly flexible reduced graphene oxide@polypyrrole-polyethylene glycol foam for supercapacitors. *RSC Adv.* **10**, 29090-29099 (2020).

40 Wickramathilaka, M. P. & Tao, B. Y. Characterization of covalent crosslinking strategies for synthesizing DNA-based bioconjugates. *J. Biol. Eng.* **13**, 1-10 (2019).

41 Carl, P., Ramos, II, Segundo, M. A. & Schneider, R. J. Antibody conjugation to carboxyl-modified microspheres through N-hydroxysuccinimide chemistry

for automated immunoassay applications: A general procedure. *Plos One.* **14**, 1-18 (2019).

42 Cao, Y. *et al.* Assessing the activity of antibodies conjugated to upconversion nanoparticles for immunolabeling. *Anal. Chim. Acta.* **1209**, 1-9 (2022).

43 Sarita Devi, S. R., Sarah Döring, Lukas Hiller, Archana Kaliyaraj Selva Kumar, Sabine Flemig, Chandan Singh, Zoltán Konthur, Vasile-Dan Hodoroaba and Rudolf J. Schneider. Antibodies Functionalized Magnetic Fe-Metal-Organic Framework Based Biosensor for Electrochemical Detection of Tetanus NeuroToxin. *Sens. Actuators B Chem.* **431**, 1-35 (2025).

44 Chen, X., Dai, Q., Qiu, X., Luo, X. & Li, Y. New nanosensor fabricated on single nanopore electrode filled with prussian blue and graphene quantum dots coated by polypyrrole for hydrogen peroxide sensing. *Talanta.* **274**, 1-7 (2024).

45 Guettiche, D. *et al.* One-step electrosynthesis of a nanocomposite of functionalized graphene and polypyrrole for enhanced room-temperature nitrogen oxide sensing. *J. Polym. Sci.* **62**, 5317-5331 (2024).

46 Nguyen, M. B. *et al.* A novel bimetallic MOFs combined with gold nanoflakes in electrochemical sensor for measuring bisphenol A. *RSC Adv.* **12**, 33825-33834 (2022).

47 Jamshidi, M., Walcarius, A., Thangamuthu, M., Mehrgardi, M. & Ranjbar, A. Electrochemical approaches based on micro- and nanomaterials for diagnosing oxidative stress. *Microchim. Acta.* **190**, 117-149 (2023).

48 Oleneva, E. *et al.* A Simple Procedure to Assess Limit of Detection for Multisensor Systems. *Sensors.* **19**, 1-11 (2019).

49 Li, J. *et al.* Programming an Amplified and Self-Calibrated Electrochemical Biosensor with High Sensitivity, Reproducibility, and Stability for ORAOV 1 Detection. *Anal. Chem.* **97**, 3449-3457 (2025).

50 G, S. C., Gokavi, L., Ravikumar, C. H. & Balarkishna, R. G. Antibody-modified 2D MXene nanosheet probes for selective, picolevel detection of cancer biomarkers. *Biosens. Bioelectron.* **271**, 1-9 (2025).

51 Campuzano, S., Pedrero, M., Yáñez-Sedeño, P. & Pingarrón, J. M. Antifouling (Bio)materials for Electrochemical (Bio)sensing. *Int. J. Mol. Sci.* **20**, 1-19 (2019).

52 Kohl, Y. *et al.* Rapid identification of in vitro cell toxicity using an electrochemical membrane screening platform. *Bioelectrochemistry.* **153**, 108467 (2023).

53 Robin, P. & Gerber-Lemaire, S. Design and Preparation of Sensing Surfaces for Capacitive Biodetection. *Biosensors.* **13**, 1-22 (2022).

54 Fazlali, F. *et al.* Electrochemiluminescent biosensor for ultrasensitive detection of lymphoma at the early stage using CD20 markers as B cell-specific antigens. *Bioelectrochemistry.* **138**, 107730, (2021).

55 Salvo, P. *et al.* Biosensors for Detecting Lymphocytes and Immunoglobulins. *Biosensors.* **10**, 155 (2020).

56 Białas, K. *et al.* Electrochemical microfluidic biosensor for the detection of CD4+ T cells. *Microsyst. Nanoeng.* **11**, 1-13 (2025).

57 Wang, X. *et al.* Lewis Acid-Boosted Nanozyme for In Situ Metallization Electrochemical Sensing of Extracellular Vesicles. *ACS Appl. Mater. Interfaces.* **17**, 36433-36443 (2025).

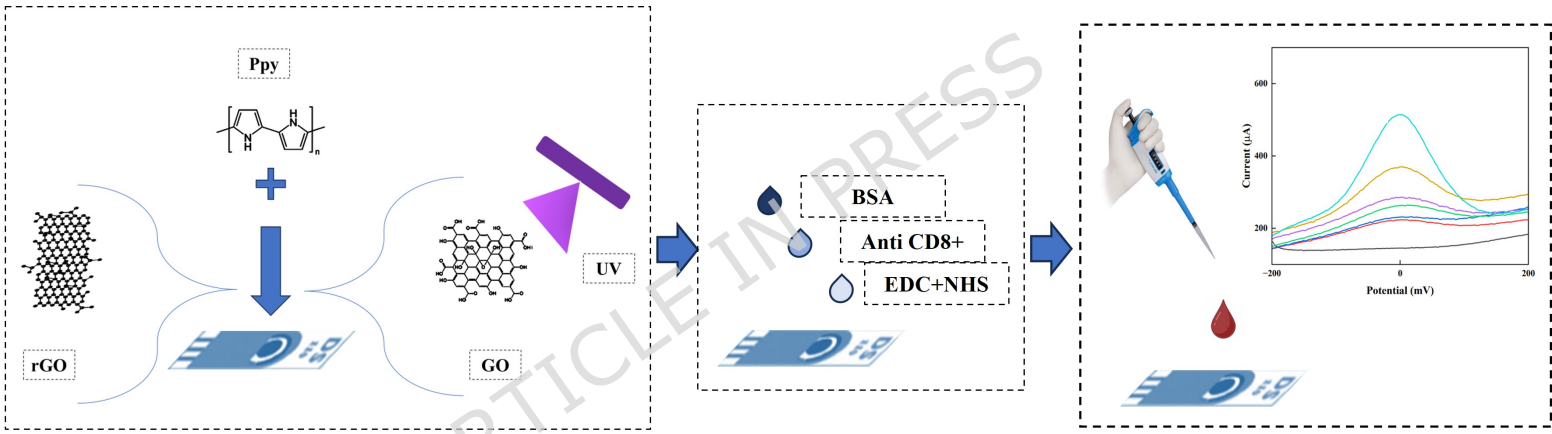

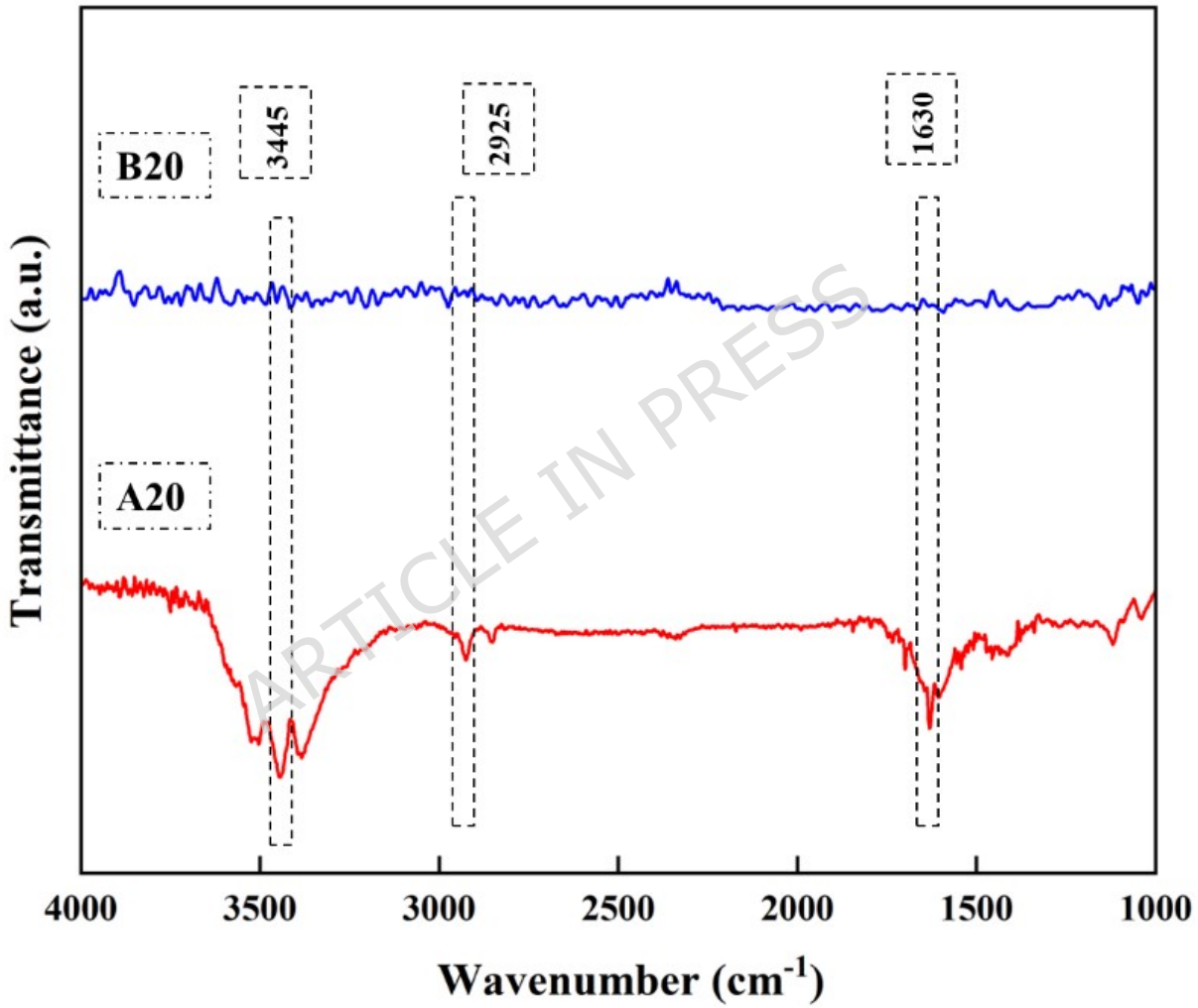

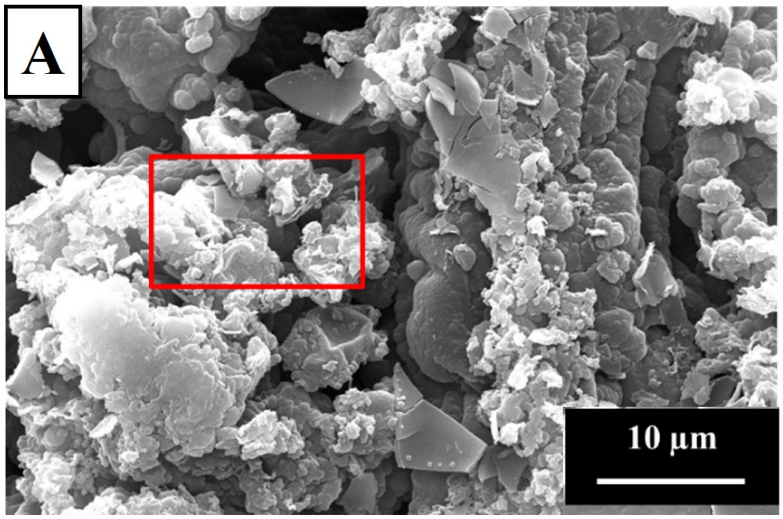

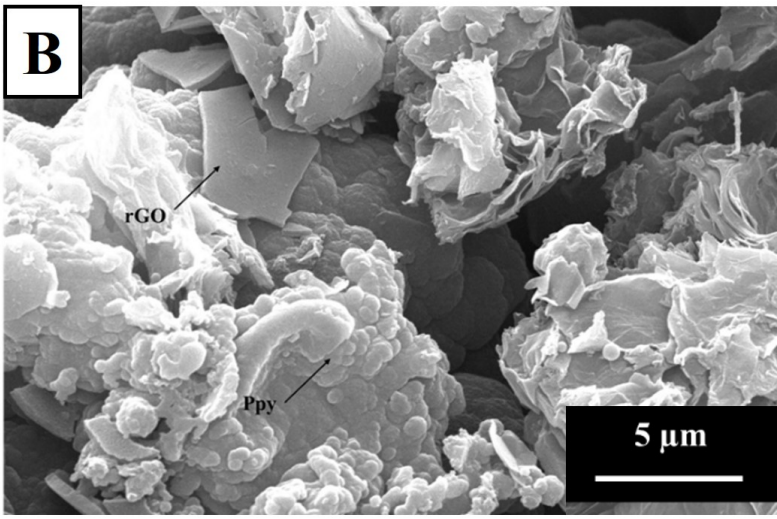

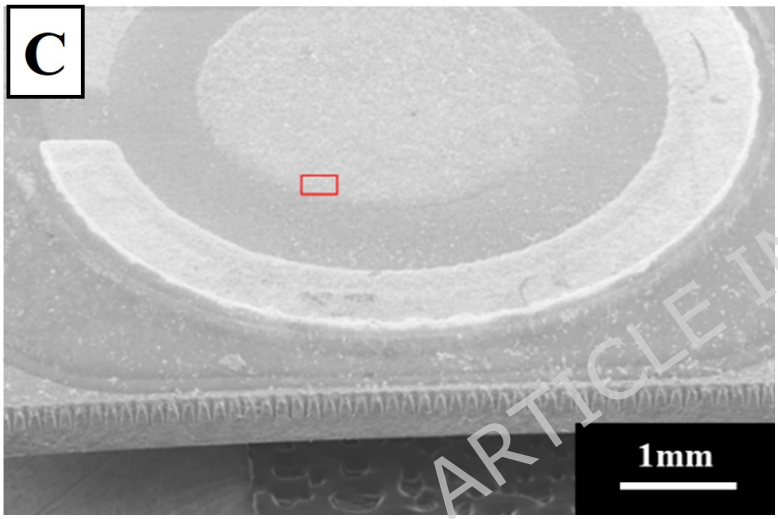

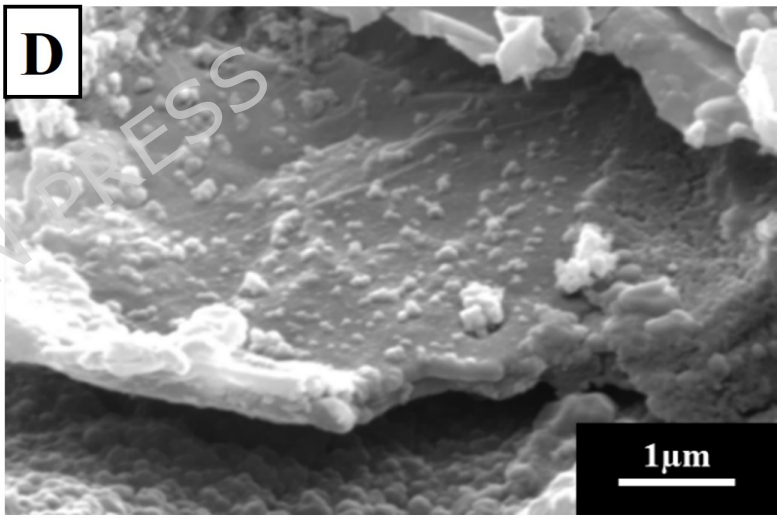

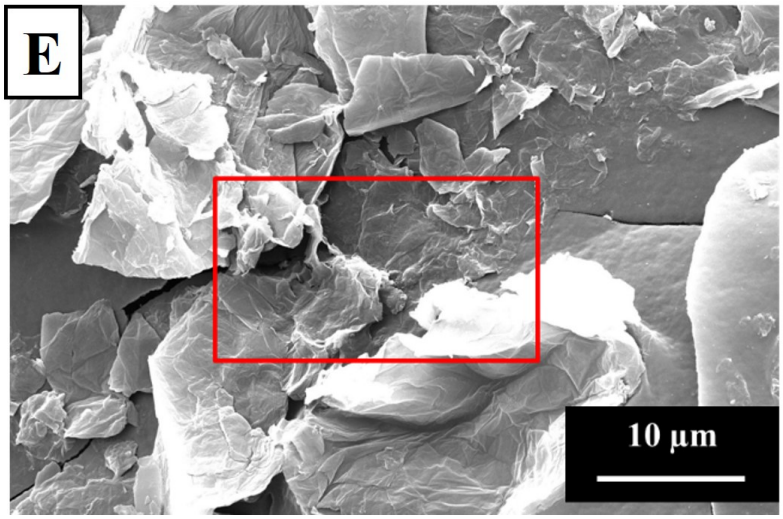

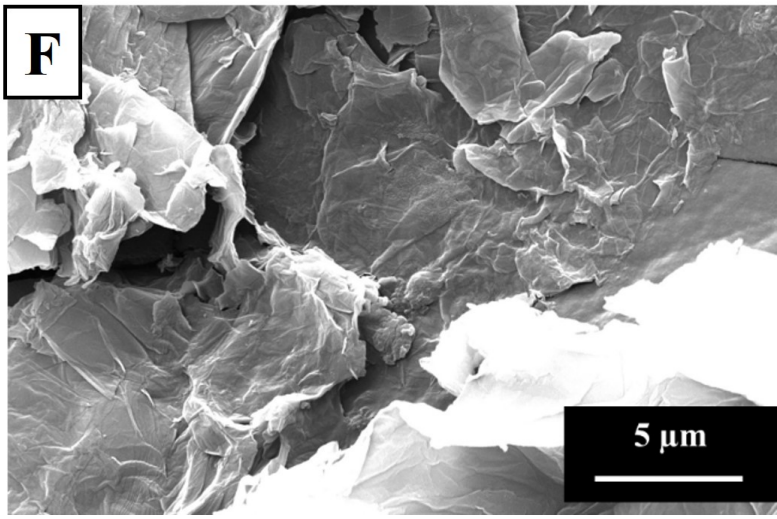

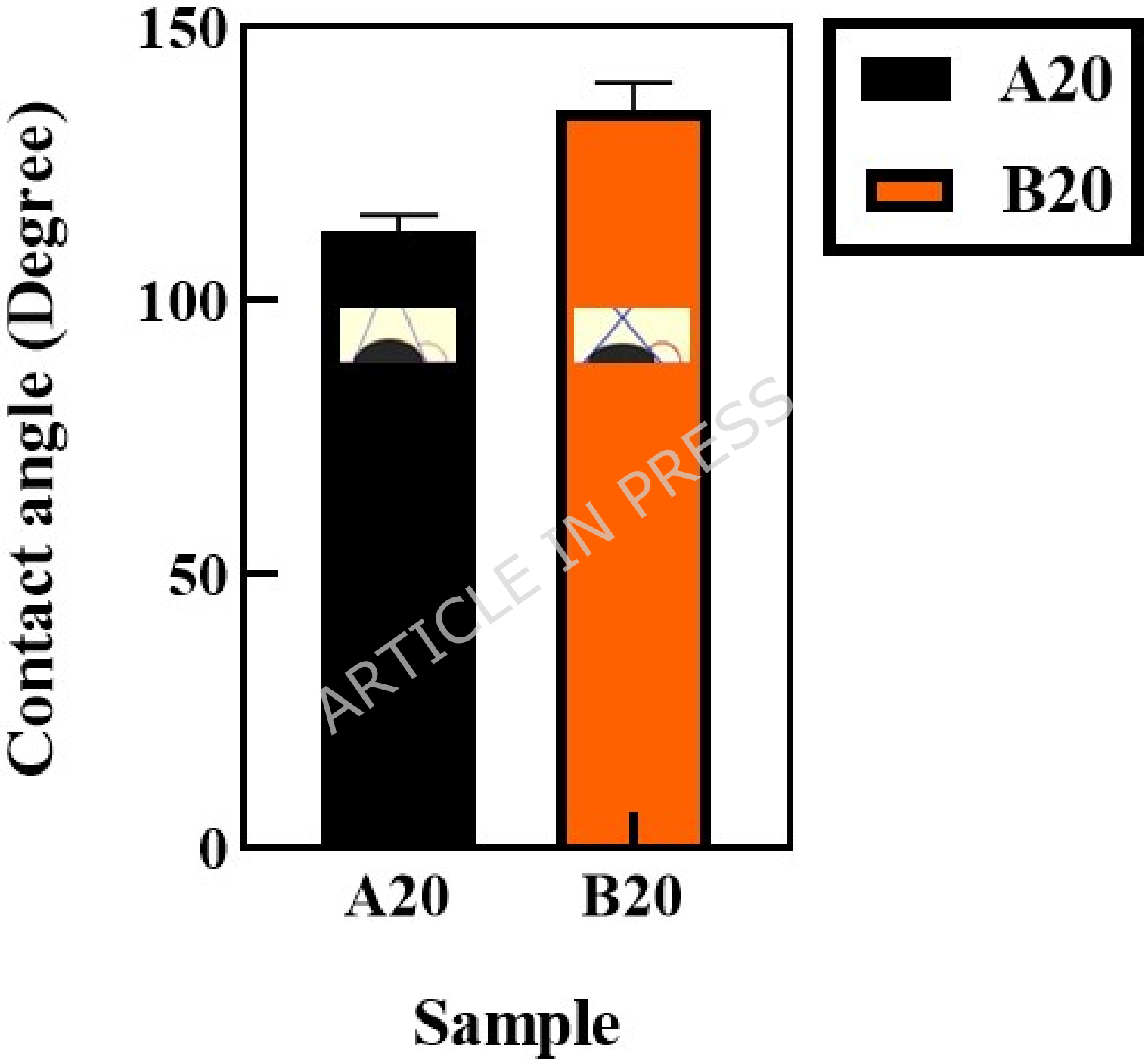

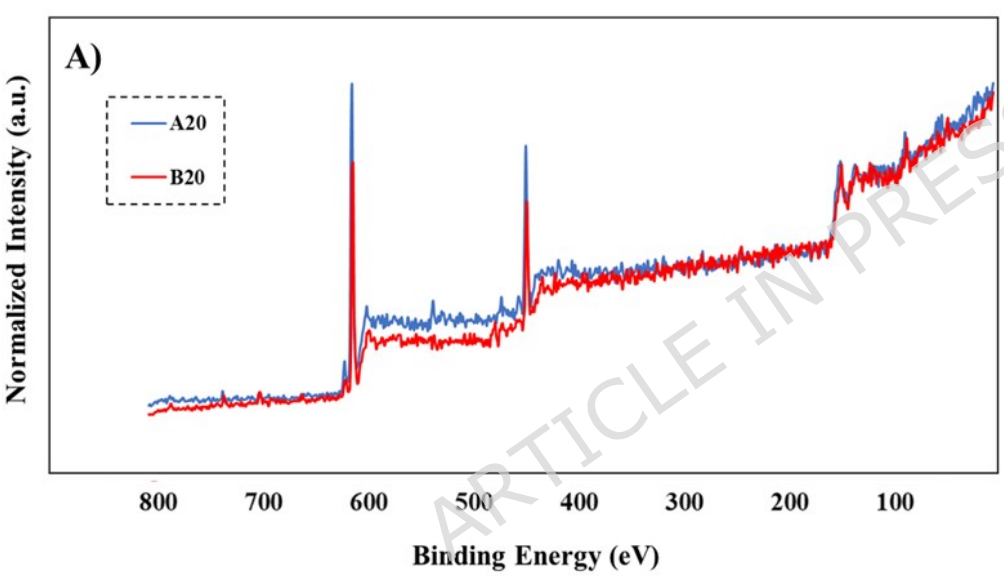

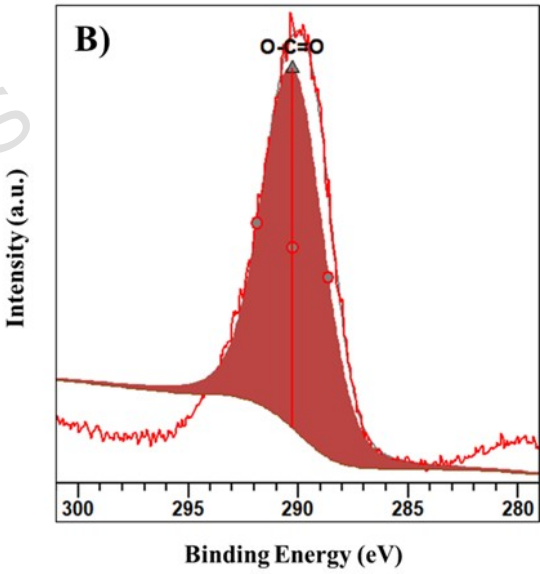

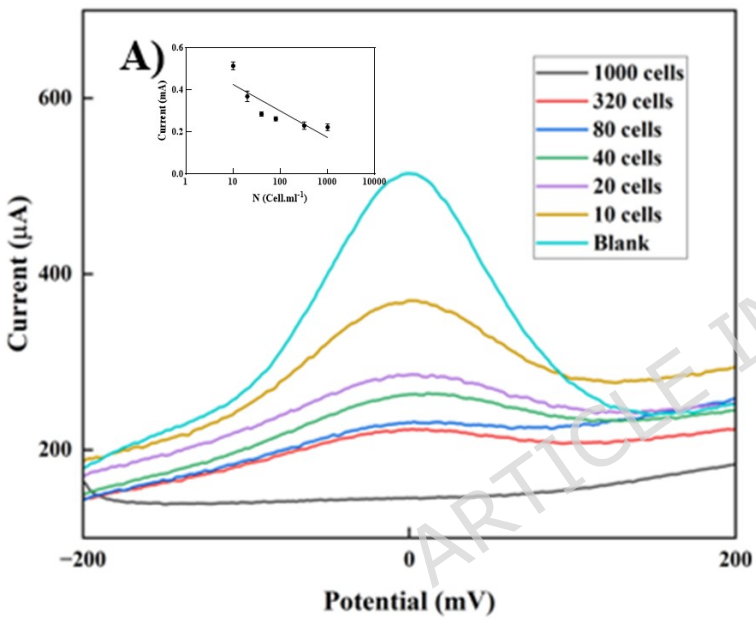

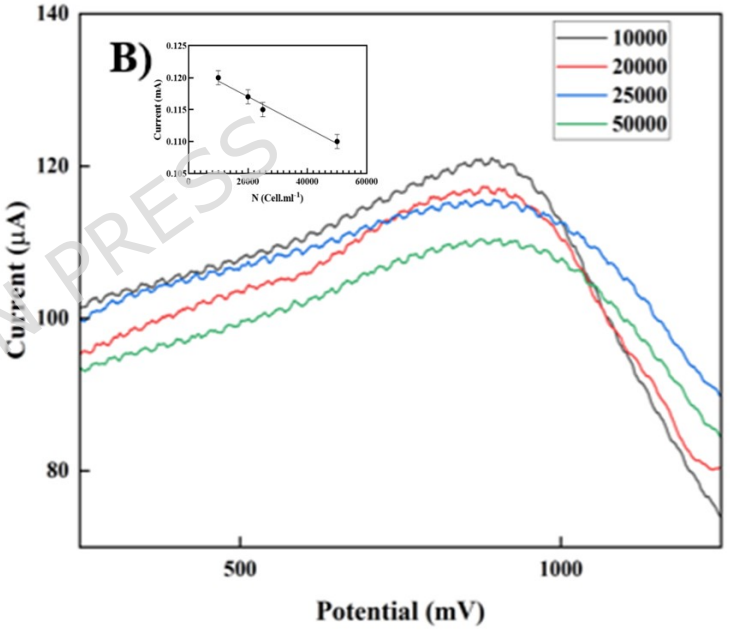

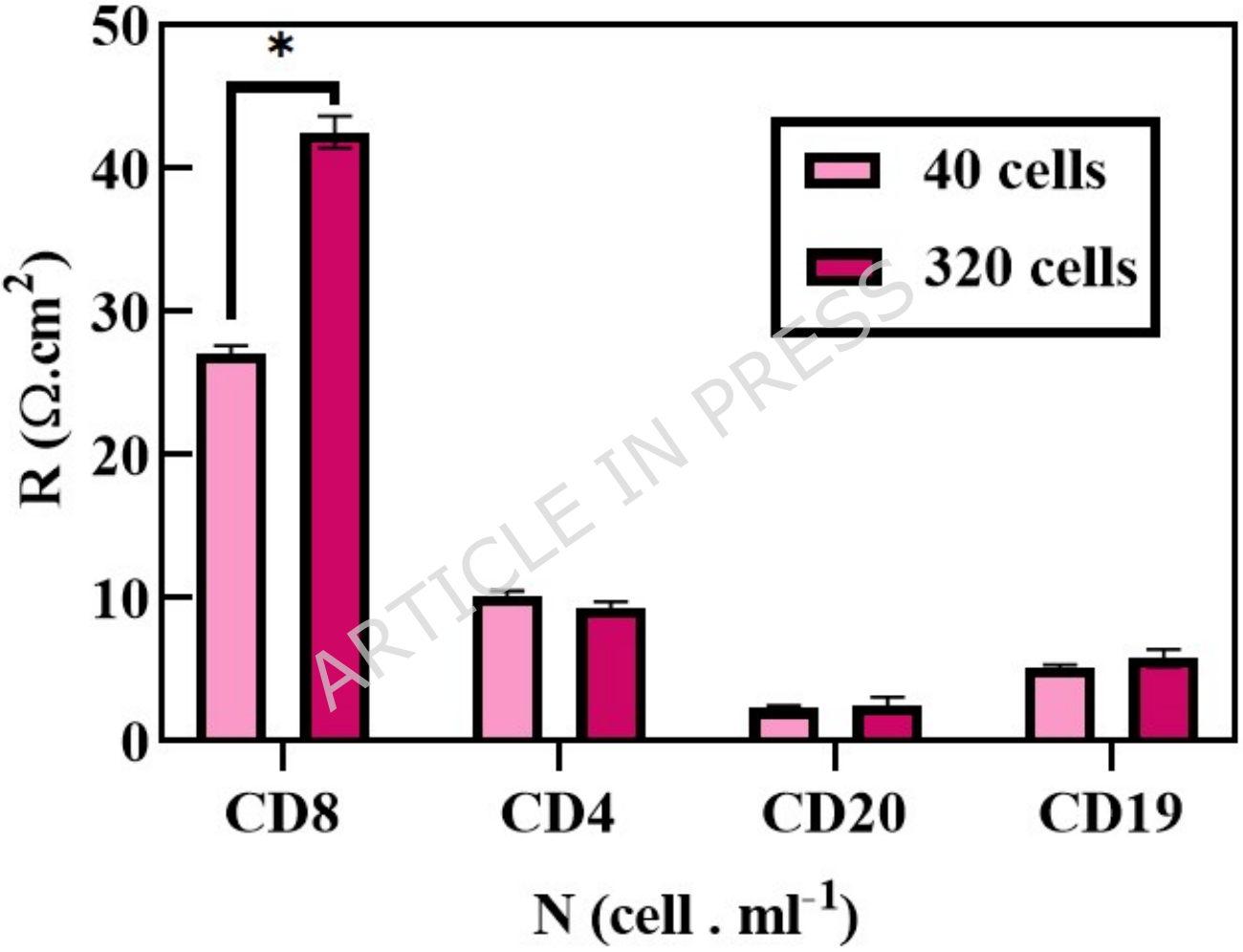

Comparing UV-Enhanced and Direct Reduction Strategies for CD8⁺ T-Cell Electrochemical Detection

Table 1: Comparison and result of recovered CD8+ T-Cell

Sample	Flowcytometry Concentration (cell.mL^{-1})	Electrochemical Concentration (cell.mL^{-1})	Recovery (%)
H1	5650	5529	97 ± 2
H2	2800	2874	96 ± 1
H3	3090	3211	96 ± 1
H4	4220	4355	96 ± 2